2023 IEEE/ASME International Conference on Advanced Intelligent Mechatronics (AIM)

Design and Parametric Analysis of a Magnetic Leadscrew with an Embedded Displacement Sensor

Wenjing Li, *Student Member* and Kok-Meng Lee*, Life Fellow, IEEE*

***Abstract*—Rotary to translational transmission systems play an important role in many applications from engineering to human assistance devices. Although lead and ball screws are widely available, they suffer mechanical wear/tear problems due to contact friction. Motivated by increasing demands for energy-efficient mechanisms for mobile and wearable robotic systems, this paper presents an analytical method to design a magnetic-leadscrew (MLS) with embedded sensing. MLS is driven by permanent magnets (PMs) converting magnetic energy to thrust forces while transmitting the rotary-to-translation motion. However, existing designs generally assume an infinitely long MLS, so its magnetic field distribution is axisymmetric and periodic. To relax these assumptions for applications that require maintaining a constant lead over a short travel, the paper formulates the magnetic field and radial/thrust forces of an MLS in closed form using a distributed current source (DCS) method for developing MLS with an embedded field-based sensing system. The sensing method determines the unique solution to the inverse magnetic field model and measures the translation and rotation independently. With the DCS models, a parametric study has been conducted numerically leading to the development of a prototype PM-driven MLS with embedded sensing, upon which the magnetic field model, sensing system, and algorithm are numerically illustrated and experimentally validated.**

***Index Terms*— Magnetic leadscrew, electromagnetics, sensor, helical magnetic field, force model, permanent magnet.**

I. INTRODUCTION

Linear actuators providing thrust forces and displacements are widely used in many robotic applications ranging from manufacturing, automotive, and aerospace industries [1][2] to emerging fields, particularly the increasing demands for human assistance devices and rehabilitation exoskeletons [3][4] where compliance must be appropriately designed to accommodate natural variations within human joints. Mechanical lead and ball screws that take advantage of low cost highly efficient electric motors to convert rotation-to-translation motions are commonly used with a built-in spring mechanism; however, their performances are limited by common wear/tears between moving contact elements and their accompanied backlash and other nonlinear uncertainties. To overcome problems associated with mechanical spring-loaded leadscrews (for example, vehicle active suspension system [5]), a magnetic leadscrew (MLS) composed of helical-shaped PMs in the translator and rotor has been employed as an alternative for its high force density and energy efficiency. Recent research has continued to demonstrate promising properties of magnetic lead screws for applications such as a wave energy converter [6] designed to harvest energy from ocean wave motion. Compared with its mechanical counterparts, PM-driven MLS has the merits of inherent overload protection, minimal friction, and a low need for maintenance because of contact-free transmission via a magnetic field; more importantly, it offers natural compliance by the virtue of the magnetic repulsion between the embedded PMs that requires no external power but can be externally controlled by its motorized driver. However, the potentials of MLS have been underexploited due to the lack of effective modeling methods and embedded sensors to analyze its magnetic fields and forces for applications (requiring a short-travel range but precision force and motion control are of interest), where the end effects on the radial and thrust forces may not be neglected. For example, the MLS is part of a linear force controllable actuator in [7] and a series elastic actuator in [8], which must be capable of fine manipulation. For this reason, this paper presents an analytical method to design MLS with embedded sensing and understand its parametric effects on dynamic behaviors for motion control.

The analytical solutions to the magnetic flux density (MFD) and thrust force of an ideal MLS have been first presented in [9] with two main assumptions; 1) the axial length is infinite so that the MFD field distribution is axisymmetric and periodic; and 2) the armature is slot-less and the permeability of the iron is infinite so that the magnetic field and force problems can be reduced to two-dimensional. With these assumptions, the analytical solutions were validated in [9][10] with data simulated using the finite element method (FEM) and used in the design of an MLS-based active suspension system for vehicles [11] and more recently for design optimization of an MLS with helical PM-poles [12]. Although the commercially available FEM is a widely used numerical tool to analyze and optimize designs with complicated topologies, it must enclose relatively large airspace around the magnetic structure being analyzed. As a result, the FEM solutions to an electromagnetic model are less computationally efficient and generally prone to numerical errors [13][14] than the analytical solutions which are, unfortunately, limited to problems with simple geometry. To take the advantage of both the FEM and analytical solutions, the distributed current source (DCS) method first proposed in [15] discretizes the electromagnetic structure into elemental volume and/or surface current sources without the need to enclose the surrounding airspace and solves for its solutions in a closed form. The DCS models formulated using physical variables are useful as a design tool for optimizing various types of actuators [16], developing magnetic sensors [13], and analyzing the parametric effects on eddy-current sensing [14].

To relax the assumptions commonly made in the traditional analyses of an MLS, this paper presents an analytical DSC method to model the MLS's magnetic field/forces, and an embedded sensing system utilizing the existing magnetic fields

This work was supported in part by the U.S. National Science Foundation under Grant CMMI-1662700, and in part by the Georgia Tech IRIM Seed Grant DE00020148. *Corresponding author: Kok-Meng Lee*

W. Li and K.-M. Lee are with the George W. Woodruff School of Mechanical Engineering, Georgia Institute of Technology, Atlanta, GA 30332 USA. (e-mail: kokmeng.lee@me.gatech.edu, wenjingli@gatech.edu).

to measure its rotational and translational displacements of the MLS. The remainder of this paper offers the following:

- *Section II* formulates the magnetic fields of an MLS using a DCS method for computing its radial/thrust forces in closed form and for sensing its rotational and translational motions. The DCS models relax some common assumptions; for example, negligible end effects and ideal "gear ratio".
- To gain insights into an MLS design for short-length applications, *Section III* presents three numerical studies: the *first* analyzes the end effects on the MLS using the DCS-based force model. The *second* investigates the parametric effects of the magnetic models on the field-based sensor design. The *third* presents a three-step algorithm to determine the unique solution to the inverse magnetic field model and measures the translational/rotational displacements.
- Based on the DCS models without assuming an ideal "gear ratio" and magnetization, *Section IV* presents the development of a prototype MLS with embedded sensing and experimental validation of the field-based sensing method.

II. ANALYTICAL MLS MODELS

Figure 1(a) defines the coordinate frames, components, and parameters for design and modeling a magnetic leadscrew (MLS) with an embedded sensing system, where *XYZ* is a world (reference) frame and $x_r y_r z_r$ and $x_t y_t z_t$ are the local coordinate frames of the rotor (radius r_r) and the translator (radius r_t), respectively; and the (z_r, z_t) axes are aligned with the *Z* axis. As the screw rotates (angle θ), the translator moves (displacement z) from its initial position z_0 along the rotating axis. Traditionally, the MLS design assumes a position-invariant "gear" ratio $\theta/z(=2\pi/\lambda)$ which indicates z traveled by λ as θ rotates by 2π during the rotary-to-translation transmission.

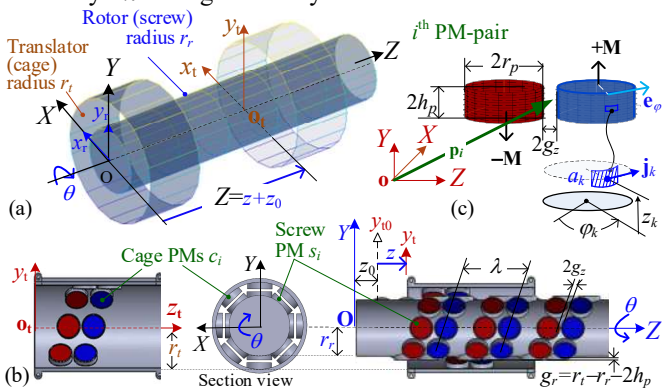

Figure 1. Schematic of Magnetic leadscrew (MLS). (a) Coordinate systems. (b) PM geometry. (c) Leadscrew parameters.

As shown in Fig. 1(b) where the circumferential surfaces of the rotor and the translator are separated by an airgap g_r, (N_r, N_t) permanent magnets (PMs) are surface mounted on the (rotor, translator) along a helix (pitch λ). The PMs with axial magnetization $\pm\mathbf{M}$ (Fig. 1c) are in pairs separated by a gap of $2g_z$ and, without loss of generality, they are assumed to have a cylindrical geometry (radius r_p and thickness $2h_p$) in the following discussion. For a complete helix that has *N* PM-pairs, the (position $\mathbf{p}_{cl}$, magnetization $\mathbf{n}_{cl}$) vectors of the l^{th} PM-pair have the form in the local coordinates in (1a, b) where the subscript c (= r or t) denotes the (rotor or translator):

$$\mathbf{p}_{cl\pm}=\begin{bmatrix} r_c\cos(l\phi) \\ r_c\sin(l\phi) \\ l\lambda/N \pm (r_p+g_z)\end{bmatrix} \text{ and } \mathbf{n}_{cl}=\begin{bmatrix}\cos(l\phi)\\ \sin(l\phi)\\ 0\end{bmatrix} \tag{1a, b}$$

$$\phi=\frac{2\pi}{N} \text{ and } l=\begin{cases} i=0,1,\cdots,(N_r-1) & \text{Rotor} \\ j=0,1,\cdots,(N_t-1) & \text{Translator}\end{cases}. \tag{1c}$$

For analyzing the magnetic system, the cylindrical PM (magnetization $\mathbf{M} = M_0\mathbf{n}_{cl}$) in the air is modeled as a surface current density (SCD) $\mathbf{K}$ source to account for its boundary effect, which can be computed from the cross-product of the circumferential surface-normal $\mathbf{n}_s$ and $\mathbf{M}$, providing a basis to solve for the MFD of the PM-pairs in a closed form using the DCS method [15] which decomposes the PM's circumferential surface ($a_S=4\pi h_p r_p$) into N_K SCD $\mathbf{k}_k$ elements (each with an area $a_k=a_s/N_k$ where $k=1, 2, \ldots, N_k$). Its MFD can then be computed by superposition reducing the computing of the Biot-Savart surface integral to a summation.

In *XYZ* coordinates, the DCS-modeled MFD $\mathbf{B}_l$ of the l^{th} PM-pair at a point $\mathbf{P}$ is given by (2a~g) where the subscribes $\pm$ denote the $\pm\mathbf{M}$ and the position vector $\mathbf{P}_{lk}$ locates the k^{th} elemental SCD $\mathbf{K}_{ik}$ of the l^{th} PM-pair:

$$\mathbf{B}_l(\mathbf{P})=\sum_{k=1}^{N_k}\left[\mathbf{B}_{lk+}(\mathbf{P},\mathbf{P}_{lk+})+\mathbf{B}_{lk-}(\mathbf{P},\mathbf{P}_{lk-})\right] \tag{2a}$$

$$\text{where } \mathbf{B}_{lk\pm}(\mathbf{P},\mathbf{P}_{lk\pm})=\frac{\mu_0}{4\pi}\frac{\mathbf{K}_{lk\pm}a_k\times(\mathbf{P}-\mathbf{P}_{lk\pm})}{|\mathbf{P}-\mathbf{P}_{lk\pm}|^3} \tag{2b}$$

$$\mathbf{P}_{lk\pm}=[\mathbb{R}_c]\begin{bmatrix}C_{\varphi k}\\ S_{\varphi k}\\ z_k\end{bmatrix}+\mathbf{P}_{cl\pm},\ \begin{bmatrix}C_{(*)}\\ S_{(*)}\end{bmatrix}=\begin{bmatrix}\cos(*)\\ \sin(*)\end{bmatrix} \tag{2c}$$

$$\text{and } \mathbf{K}_{lk\pm}=-[\mathbb{R}_c]\begin{bmatrix}C_{\varphi k}\\ S_{\varphi k}\\ 0\end{bmatrix}\times(\pm\mathbf{M}) \tag{2d}$$

$$\text{and where } [\mathbb{R}_c]=\begin{cases}[\mathbf{R}_z(i\phi+\theta)][\mathbf{R}_y(\pi/2)] & c=r\\ [\mathbf{R}_z(j\phi)][\mathbf{R}_y(\pi/2)] & c=t\end{cases} \tag{2e}$$

$$\left[\mathbf{R}_y\left(\frac{\pi}{2}\right)\right]=\begin{bmatrix}0&0&1\\0&1&0\\-1&0&0\end{bmatrix};\ \mathbf{R}_z(\bullet)=\begin{bmatrix}\cos(\bullet)&-\sin(\bullet)&0\\ \sin(\bullet)&\cos(\bullet)&0\\0&0&1\end{bmatrix} \tag{2f, g}$$

In (2c), the position vector $\mathbf{P}_{cl\pm}$ can be described by (3a, b) where the local coordinates $\mathbf{p}_{ri\pm}$ and $\mathbf{p}_{tj\pm}$ are given by (1a~c):

$$\mathbf{P}_{ri\pm}(\theta)=\begin{bmatrix}X_{ri\pm}(\theta)\\ Y_{ri\pm}(\theta)\\ Z_{ri\pm}\end{bmatrix}=\mathbf{R}_z(\theta)\mathbf{p}_{ri\pm} \tag{3a}$$

$$\mathbf{P}_{tj\pm}(Z)=\begin{bmatrix}X_{tj}\\ Y_{tj}\\ Z_{tj}(Z)\end{bmatrix}=\begin{bmatrix}0\\0\\z+z_0\end{bmatrix}+\mathbf{p}_{tj\pm} \tag{3b}$$

To facilitate design, the geometrical parameters are normalized to the PM radius r_p in (4a~e):

$$\frac{h_p}{\rho_p r_p}=\frac{r_t}{\rho_t r_p}=\frac{\lambda}{\rho_\lambda r_p}=\frac{g_z}{\rho_z r_p}=\frac{g_r}{\rho_r r_p}=1 \tag{4a~e}$$

For consistency, the position vectors, MFD, SCD, and force are normalized accordingly in (5a~d) where (B_o, f_o) are defined in (5e, f) and μ_o is the permeability of free space:

$$\frac{\mathbf{P}}{r_p\bar{\mathbf{P}}}=\frac{\mathbf{B}}{\bar{\mathbf{B}}B_o}=\frac{\mathbf{K}}{\bar{\mathbf{K}}M_o}=\frac{\mathbf{f}}{\bar{\mathbf{f}}f_o}=\mathbf{I}_{3\times3} \tag{5a~d}$$

$$\text{where } B_o=\mu_o M_o \text{ and } f_o=B_o M_o a_S \tag{5e, f}$$

With the normalized parameters and variables defined in (4a~e) and (5a~d), the force models and magnetic field for designing an MLS and its embedded sensor are described in *Sections II.A* and *II.B*, respectively.

A. Magnetic Force Model of the MLS

Using the DCS models (2a~g), the volume integral for calculating the Lorentz force exerted on the translator reduces to a summation of elemental cross-products ($\mathbf{K}_{iK} \times \mathbf{B}_r$) over the N_K elements. For clarity, the indexes (K, k) are used to indicate the SCD elements of the (rotor, translator). Since the SCD vector $\mathbf{K}_{tk}$ is directly used in the rotor field $\mathbf{B}_r$, it is not necessary to compute the MFD generated by the current loop. In the *XYZ* coordinates, the normalized magnetic force acting on the translator (consisting of N_t PM-pairs) can be computed from the sum of the individual forces given by (6a, b):

$$\bar{\mathbf{f}}(\theta,z)=\frac{1}{N_K}\sum_{j=0}^{N_t-1}\sum_{k=1}^{N_K}\left[\bar{\mathbf{K}}_{jk+}\times\bar{\mathbf{B}}_r\left(\bar{\mathbf{P}}_{jk+}\right)+\bar{\mathbf{K}}_{jk-}\times\bar{\mathbf{B}}_r\left(\bar{\mathbf{P}}_{jk-}\right)\right] \tag{6a}$$

where $\bar{\mathbf{B}}_r\left(\bar{\mathbf{P}},\ \theta\right)=\left[\bar{B}_{rx}\quad \bar{B}_{ry}\quad \bar{B}_{rz}\right]^{\mathrm{T}}$

$$\frac{\rho_p}{N_k}\sum_{i=0}^{N_t-1}\sum_{K=1}^{N_K}\left(\frac{\bar{\mathbf{K}}_{iK+}\times\left(\bar{\mathbf{P}}-\bar{\mathbf{P}}_{iK+}\right)}{\left|\bar{\mathbf{P}}-\bar{\mathbf{P}}_{iK+}\right|^3}+\frac{\bar{\mathbf{K}}_{iK-}\times\left(\bar{\mathbf{P}}-\bar{\mathbf{P}}_{iK-}\right)}{\left|\bar{\mathbf{P}}-\bar{\mathbf{P}}_{iK-}\right|^3}\right) \tag{6b}$$

$$\bar{\mathbf{K}}_{iK+}=-\bar{\mathbf{K}}_{iK-}=\left[-C_{\varphi K}S_{i\phi+\theta}\quad C_{\varphi K}C_{i\phi+\theta}\quad S_{\varphi K}\right]^{\mathrm{T}} \tag{6c}$$

$$\bar{\mathbf{K}}_{jk+}=-\bar{\mathbf{K}}_{jk-}=\left[-C_{\varphi k}S_{j\phi}\quad C_{\varphi k}C_{j\phi}\quad S_{\varphi k}\right]^{\mathrm{T}} \tag{6d}$$

$$\mathbf{P}_{iK\pm}=\begin{bmatrix}C_{i\phi+\theta}\left(\rho_r+\bar{z}_K\right)-S_{i\phi+\theta}S_{\varphi K}\\ S_{i\phi+\theta}\left(\rho_r+\bar{z}_K\right)+C_{i\phi+\theta}S_{\varphi K}\\ i\rho_\lambda/N+C_{\varphi K}\end{bmatrix}+\begin{bmatrix}0\\0\\\pm(1+\rho_z)\end{bmatrix} \tag{6e}$$

$$\text{and }\mathbf{P}_{jk\pm}=\begin{bmatrix}C_{j\phi}\left(\rho_t+\bar{z}_k\right)-S_{j\phi}S_k\\ S_{j\phi}\left(\rho_t+\bar{z}_k\right)+C_{j\phi}S_{\varphi k}\\ j\rho_\lambda/N+C_{\varphi k}\end{bmatrix}+\begin{bmatrix}0\\0\\\bar{Z}\pm(1+\rho_z)\end{bmatrix} \tag{6f}$$

As illustrated in Fig. 2, the denominators in (6b) are the distances (7a, b) between the j^{th} translator and i^{th} rotor PM-pairs:

$$\bar{L}_{++}=\left|\bar{\mathbf{L}}_{++}\right|=\left|\bar{\mathbf{P}}_{jk+}-\bar{\mathbf{P}}_{iK\pm}\right|;\ \bar{L}_{-\pm}=\left|\bar{\mathbf{L}}_{-\pm}\right|=\left|\bar{\mathbf{P}}_{jk-}-\bar{\mathbf{P}}_{iK\pm}\right| \tag{7a, b}$$

In (7a, b), the subscripts [(++ and −−), (+− and −+)] indicate the magnetization vectors of the PM-pairs contributing to [repulsive, attractive] forces. Since the magnetization vectors of both the rotor PMs and translator PMs are radially pointing in the *XY* plane, the line connecting the two centers of the j^{th} translator PM-pair is always parallel to that of the i^{th} rotor PM-pair. Hence, the two lines between the (j^{th} translator and i^{th} rotor) PMs with $\mathbf{M}_+$ and that with $\mathbf{M}_-$, which contribute to repulsive forces, are parallel and have equal lengths:

$$L_{++}=L_{--} \tag{7c}$$

The numerators in (6a, b) can be written as dot products (8a) in terms of that have the properties given by (8b~e):

$$\bar{\mathbf{K}}_{jk\pm}\times\bar{\mathbf{K}}_{iK\pm}\times\left(\bar{\mathbf{P}}_{jk\pm}-\bar{\mathbf{P}}_{iK\pm}\right)=\left[\bar{\mathbf{K}}_{jk\pm}\bullet\left(\bar{\mathbf{P}}_{jk\pm}-\bar{\mathbf{P}}_{iK\pm}\right)\right]\bar{\mathbf{K}}_{iK\pm}-\left[\bar{\mathbf{K}}_{iK\pm}\bullet\bar{\mathbf{K}}_{jk\pm}\right]\left(\bar{\mathbf{P}}_{jk+}-\bar{\mathbf{P}}_{iK\pm}\right) \tag{8a}$$

$$\bar{\mathbf{K}}_{jk+}\bullet\left(\bar{\mathbf{P}}_{jk+}-\bar{\mathbf{P}}_{iK+}\right)=-\bar{\mathbf{K}}_{jk-}\bullet\left(\bar{\mathbf{P}}_{jk-}-\bar{\mathbf{P}}_{iK-}\right) \tag{8b}$$

$$\bar{\mathbf{K}}_{jk\pm}\bullet\left(\bar{\mathbf{P}}_{jk\pm}-\bar{\mathbf{P}}_{iK\mp}\right)=\pm\bar{\mathbf{K}}_{jk+}\bullet\left(\bar{\mathbf{P}}_{jk+}-\bar{\mathbf{P}}_{iK+}\right)+2S_{\varphi k}\left(1+\rho_z\right) \tag{8c}$$

$$\bar{\mathbf{K}}_{iK+}\bullet\bar{\mathbf{K}}_{jk+}=\bar{\mathbf{K}}_{iK-}\bullet\bar{\mathbf{K}}_{jk-}=-\bar{\mathbf{K}}_{iK+}\bullet\bar{\mathbf{K}}_{jk-}=-\bar{\mathbf{K}}_{iK-}\bullet\bar{\mathbf{K}}_{jk+} \tag{8d}$$

For compactness and gaining physically intuitive insights into the magnetic forces (6a) can be written as (9a~e):

$$\bar{\mathbf{f}}(\theta,z)=\frac{\rho_p}{N_KN_k}\sum_{j,k}\sum_{i,K}\begin{bmatrix}2\bar{L}_{++}^{-3}\left(a_{j++}\bar{\mathbf{K}}_{iK+}-b_{j++}\bar{\mathbf{L}}_{++}\right)+\\ \bar{L}_{+-}^{-3}\left(a_{j+-}\bar{\mathbf{K}}_{iK-}-b_{j+-}\bar{\mathbf{L}}_{+-}\right)+\\ \bar{L}_{-+}^{-3}\left(a_{j-+}\bar{\mathbf{K}}_{iK+}-b_{j-+}\bar{\mathbf{L}}_{-+}\right)\end{bmatrix} \tag{9a}$$

where $a_{j++}=\bar{\mathbf{K}}_{jk+}\bullet\bar{\mathbf{L}}_{++}$, $a_{j\pm\mp}=\bar{\mathbf{K}}_{jk\pm}\bullet\bar{\mathbf{L}}_{\pm\mp}$ (9b, c)

$$b_{j++}=\bar{\mathbf{K}}_{iK+}\bullet\bar{\mathbf{K}}_{jk+}\ \text{ and }\ b_{j\pm\mp}=\bar{\mathbf{K}}_{iK\pm}\bullet\bar{\mathbf{K}}_{jk\mp} \tag{9d, e}$$

Using the properties (8b~d), (9a) can be expressed as

$$\bar{\mathbf{f}}(\theta,z)=\frac{\rho_p}{N_KN_k}\sum_{j,k}\sum_{i,K}\left[\alpha_{ij}\bar{\mathbf{K}}_{iK+}+\beta_{ij}\bar{\mathbf{L}}_{++}+\boldsymbol{\gamma}_{ij}\right] \tag{10a}$$

where $\alpha_{ij}=L_{eq}^{-3}a_{j++}+2\left(1+\rho_z\right)L_{A-}^{-3}S_{\varphi k}$, (10b)

$$\beta_{ij}=L_{eq}^{-1}b_{j++},\ \boldsymbol{\gamma}_{ij}=2L_{A-}^{-1}\left(1+\rho_z\right)S_{\varphi k}\begin{bmatrix}0\\0\\1\end{bmatrix} \tag{10c, d}$$

$$L_{eq}^{-3}=2L_{++}^{-3}-L_{-+}^{-3}-L_{+-}^{-3}\ \text{ and }\ L_{A-}^{-3}=L_{-+}^{-3}-L_{+-}^{-3}. \tag{10e, f}$$

The model (10a~f) provides the basis to analyze the effects of the MLS parameters, (r_p, h_p; M_o), (r_t, r_r, g_z, λ) and the magnetic lead z_0 (Fig. 1b), on the force **f**; a good understanding is essential to maintain a position-invariant gear ratio for rotary-to-translation transmission while minimizing the radial force.

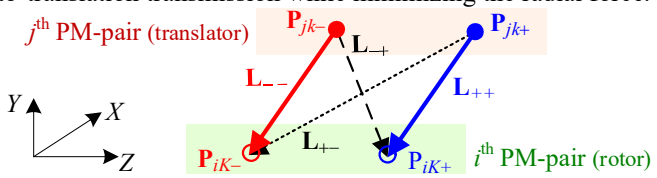

Fig. 2 Schematics illustrating the elemental force model (6a).

B. Translator MFD Models for Embedded Motion Sensing

For (Z, θ) motion sensing of the MLS, the embedded motion sensing system measures the translator MFD obtained by subtracting the rotor MFD from measurements. As in (6b), the MFD field of the translator-PMs at the sensing point $\bar{\mathbf{P}}_s$ can be computed from the cross-products over the N_k elements, which can be rewritten in normalized form as

$$\bar{\mathbf{K}}_{jk\pm}\times\left(\bar{\mathbf{P}}_s-\bar{\mathbf{P}}_{jk\pm}\right)=\left[\mathbf{skew}\left(\bar{\mathbf{K}}_{jk\pm}\right)\right]\left(\bar{\mathbf{P}}_s-\bar{\mathbf{P}}_{jk\pm}\right) \tag{11a}$$

$$\text{where }\mathbf{skew}\left(\mathbf{v}=\begin{bmatrix}v_x\\v_y\\v_z\end{bmatrix}\right)=\begin{bmatrix}0&-v_z&v_y\\v_z&0&-v_x\\-v_y&v_x&0\end{bmatrix}, \tag{11b}$$

$$\text{and }\ \bar{\mathbf{P}}_s-\bar{\mathbf{P}}_{lk\pm}=\begin{bmatrix}\bar{X}_s-C_{l\phi}\bar{z}_k+S_{l\phi}S_{\varphi k}-\bar{x}_{cl}\\ \bar{Y}_s-S_{l\phi}\bar{z}_k-C_{l\phi}S_{\varphi k}-\bar{y}_{cl}\\ \left(\bar{Z}_s-\bar{Z}\right)+C_{\varphi k}-\bar{z}_{cl\pm}\end{bmatrix} \tag{11c}$$

For simplicity, we define

$$\Sigma_{l\pm}(\bullet)=\sum_{k=1}^{N_k}\frac{\bullet}{\left[\left|\bar{\mathbf{P}}_s-\bar{\mathbf{P}}_{lk\pm}\right|^2\right]^{3/2}} \tag{12}$$

where "$\bullet$" represents ($C_{\varphi k}$ and $S_{\varphi k}$) and ($C_{\varphi k}\bar{z}_k$ and $S_{\varphi k}\bar{z}_k$) in the 1st and 2nd terms in (14), respectively. Each summation in (12) can then be compactly written as

$$\begin{aligned}\left|\bar{\mathbf{P}}_s-\bar{\mathbf{P}}_{cl\pm}\right|^2=&\left[\left(\bar{Z}_s-\bar{Z}\right)-\bar{z}_{cl\pm}\right]^2+2C_{\varphi k}\left[\left(\bar{Z}_s-\bar{Z}\right)-\bar{z}_{cl\pm}\right]+\\ &\bar{X}_s^2-2\left[\bar{x}_{cl}-\left(S_{l\phi}S_{\varphi k}-C_{l\phi}\bar{z}_k\right)\right]\bar{X}_s+\\ &\bar{Y}_s^2-2\left[\bar{y}_{cl}+\left(C_{l\phi}S_{\varphi k}+S_{l\phi}\bar{z}_k\right)\right]\bar{Y}_s+\left(\rho_c+\bar{z}_k\right)^2+1\end{aligned} \tag{13}$$

and $\sum_{k=1}^{N_K}\left[\overline{\mathbf{B}}_{lk\pm}\left(\overline{\mathbf{P}}_s,\overline{\mathbf{P}}_{lk\pm}\right)\right]=$

$$\pm\left(\begin{array}{c}\mathbf{skew}\begin{bmatrix}-S_{j\phi}\Sigma_{l\pm}(C_{\varphi k})\\ C_{j\phi}\Sigma_{l\pm}(C_{\varphi k})\\ \Sigma_{l\pm}(S_{\varphi k})\end{bmatrix}\begin{bmatrix}\overline{X}'-\overline{x}_{cl}\\ \overline{Y}'-\overline{y}_{cl}\\ \left(\overline{Z}'-\overline{Z}\right)-\overline{z}_{cl\pm}\end{bmatrix}+\\ \begin{bmatrix}1 & \Sigma_{l\pm}(S_{\varphi k}\overline{z}_k) & 0\\ -\Sigma_{l\pm}(S_{\varphi k}\overline{z}_k) & 1 & 0\\ 0 & 0 & \Sigma_{l\pm}(C_{\varphi k}\overline{z}_k)\end{bmatrix}\begin{bmatrix}C_{l\phi}\\ S_{l\phi}\\ 1\end{bmatrix}\end{array}\right) \quad (14)$$

Based on (14), the sensors are located at $\mathbf{P}_s(X_s=0,\ Y_s=0,\ Z_s)$ along the rotor centerline to determine the axial displacement. From (12) to (14), the following observations can be made:

1) The dominator of (12) reduces to

$$\left[\left|\overline{\mathbf{P}}'-\overline{\mathbf{P}}_{tj\pm}\right|^2\right]^{3/2}=\left[\begin{array}{l}\left[\left(\overline{Z}_s-\overline{Z}\right)-\overline{z}_{tj\pm}+C_{\varphi k}\right]^2+\\ S_{\varphi k}^2+\left(\rho_t+\overline{z}_k\right)^2\end{array}\right]^{3/2} \quad (15a)$$

2) Since $\sin(-\varphi k)=-\sin(\varphi k)$ and $\cos(-\varphi k)=\cos(\varphi k)$,

$$\Sigma_{j\pm}(S_{\varphi k})=\sum_{k=1}^{N_k}S_{\varphi k}\left[\left|\overline{\mathbf{P}}'-\overline{\mathbf{P}}_{jk\pm}\right|^2\right]^{-3/2}=0 \quad (15b)$$

3) The translator MFD measured by the magnetic sensors at $\mathbf{P}_s(X_s=0,\ Y_s=0,\ Z_s)$ depends only on the displacement Z:

$$\overline{\mathbf{B}}_t\left(\overline{Z}\right)=\sum_{j=0}^{N_t-1}\left[\overline{\mathbf{B}}_{tj+}\left(\overline{Z}\right)+\overline{\mathbf{B}}_{tj-}\left(\overline{Z}\right)\right] \quad (15c)$$

where $\overline{\mathbf{B}}_{tj\pm}\left(\overline{Z}\right)=$

$$\pm\left[\begin{array}{c}\left[\left(\overline{Z}_s-\overline{Z}-\overline{z}_{t\pm}\right)\Sigma_{j\pm}\left(C_{\varphi k}\right)+\Sigma_{j\pm}(1)\right]\begin{bmatrix}C_{j\phi}\\ S_{j\phi}\end{bmatrix}\\ \rho_t\Sigma_{j\pm}\left(C_{\varphi k}\right)+\Sigma_{j\pm}\left(C_{\varphi k}\overline{z}_k\right)\end{array}\right] \quad (15d)$$

The above observations suggest that Z can be measured from the Z-component of $\mathbf{B}_t$ (16a, b) assuming $r_t >> h_p$ for simplicity:

$$\frac{B_{tz}}{B_0}\left(\frac{Z-Z_s}{\lambda}\right)=\rho_t\sum_{j=0}^{N_t-1}\left[\Sigma_{j+}\left(C_{\varphi k}\right)-\Sigma_{j-}\left(C_{\varphi k}\right)\right] \quad (16a)$$

where $\Sigma_{j\pm}\left(C_{\varphi k}\right)=$

$$\sum_{k=1}^{N_k}\left\{\left[\rho_\lambda\left(\frac{Z_s-Z}{\lambda}-\frac{j}{N}\right)\mp 1+C_{\varphi k}\right]^2+S_{\varphi k}^2+\rho_t^2\right\}^{3/2} \quad (16b)$$

III. PARAMETRIC ANALYSES

The magnetic force and MFD field models (6a, b) for design analyses of the MLS and its embedded sensing system are best illustrated numerically. For a given rotor radius r_r and PM (r_p, h_p), the N PM-pairs (in a helical cycle with pitch λ) housed within the translator radius r_t with a rotor-translator airgap g_r (Fig. 1b) are constrained by (17a~c):

$$N=\text{floor}\left(\pi r_r/r_p\right);\ \rho_\lambda>4\left(1+\rho_z\right) \quad (17a, b)$$

and $\rho_t=\rho_r+2\rho_p+\rho_g$ (17c)

The nominal design, along with the values used in the studies, is given in Table I. Three numerical studies are conducted: *Section III.A* illustrates the principle and model of an MLS by simulating the parametric effects on its radial and axial (thrust) forces; the results reveal the end effects by relaxing the common assumption (18) and determining the optimal z_0. *Section III.B* analyzes the parametric effects on the MFD field of the translator PMs, which provide the theoretical basis to design an embedded sensing system for the MLS. *Section III.C* presents a method to determine the unique solution to the inverse translator-MFD model for measuring Z and θ independently.

TABLE I. Nominal values used in simulations

PM: r_p = 4.76mm, ρ_p=1/6; M_o=1.3T.

MLS: ρ_r = 3, ρ_t = 3.73, ρ_z = 0.17, ρ_λ = 6. N = 8, N_t/N = 1, N_r/N = 4, z_0/r_p =1

***Sect.* (Fig.)**	**Values used in the parametric studies**
A(Fig. 4)	N= 3, r_p = 9.53mm, ρ_p=1/6; N= 6, r_p = 6.35mm, ρ_p=1/4; N= 8, r_p = 4.76mm, ρ_p=1/3, 2/3, 4/3
A (Fig. 5)	N_t=N, N_r/N = 4, 8.
B (Fig. 6)	6c: ρ_t = 3.23, 3.73, 4.23, 4.73; ρ_λ = 4, 6, 9. 6d: ρ_λ = 5, 6, 7.

A. Parametric Effects on Magnetic Thrust Force

Traditionally, the MLS force is derived assuming (18) that generally neglects the end effects by allowing $\ell\to\pm\infty$:

$$\mathbf{f}\left(\theta=\ell\frac{2\pi}{N},z=\ell\frac{\lambda}{N}\right)\approx\mathbf{f}_0\left(Z=z_0;\theta=z=0\right) \quad (18)$$

To gain insights into the end effects of an MLS design with a short operating length, the end effects on the MLS are analyzed using the force model (10a~f).

Consider the j=0th translator PM-pair initially aligning with the i=0th rotor PM-pair. The translator PM-pairs travel along the Z axis and sequentially align with an equal number of rotor PM-pairs as the latter rotates. After translating $z=\ell\lambda/N$ or Z=z+z_0 (Fig. 1b), the j=0 translator-PMs align with the ℓ^{th} rotor-PMs while rotating $\theta=-\ell\phi$ as viewed by the translator, which can be described in the *XYZ* frame as

$$\overline{\mathbf{p}}_{t(j=0)}=\begin{bmatrix}\rho_tC_{j\phi}\\ \rho_tS_{j\phi}\\ z+\overline{z}_0\pm\left(1+\rho_z\right)\end{bmatrix}=\begin{bmatrix}\rho_t\\ 0\\ \ell\lambda/N+\overline{z}_0\pm\left(1+\rho_z\right)\end{bmatrix} \quad (19a)$$

$$\overline{\mathbf{p}}_{ri(i=\ell)}=\begin{bmatrix}\rho_rC_{(i-\ell)\phi}\\ \rho_rS_{(i-\ell)\phi}\\ \ell\lambda/N\pm\left(1+\rho_z\right)\end{bmatrix}=\begin{bmatrix}\rho_r\\ 0\\ \ell\lambda/N\pm\left(1+\rho_z\right)\end{bmatrix} \quad (19b)$$

As seen in (19a, b), the relative displacement between the j=0th translator-PM and ℓ^{th} rotor-PM in the axial direction depends only on the magnetic lead z_0, which governs the thrust force (6a, b). Figures 3 to 5 summarize the results of the numerical study to determine an optimal magnetic lead z_0 that maximizes the axial force while minimizing the radial force.

Figures 3 and 4 analyze the effects of the magnetic lead z_0 on $\mathbf{f}_0(Z=z_0;\ z=\theta=0)$. The (top, middle, bottom) plots of Fig. 3 graph the individual (f_X, f_Y, f_Z) component forces contributed by each of the translator PMs, where the (left, right) plots correspond to the PM with ($\mathbf{M}$+, $\mathbf{M}$–). Figure 4 analyzes the effects of the PM aspect ratio ρ_p and the PM-pairs/helix N on the axial and radial forces. Based on (10a~f) that relax the commonly made assumption (18), the (f_X, f_Y) acting on the j^{th} PM-pair and that on the (j+N/2)th PM-pair in the presence rotor-MFD $\mathbf{B}_r$ field are nearly equal and opposite to each other for any z_0 as shown in the 1st and 2nd rows of Fig. 3. In contrast, the j^{th} and (j+N/2)th PM-pairs contribute nearly identical f_Z in both magnitude and direction as shown in the 3rd row of Fig. 3 where all the eight (j = 0, …,7) individual contributions collapse approximately onto a single curve; the latter indicates that the magnetic force on the j^{th} PM-pair is not significantly influenced by other translator-PMs except its immediate neighbors. As a result, the net force $\mathbf{f}_0$ is primarily axial and peaked near z_0/r_p=1

(Fig. 4b) with a small but non-zero radial force (Fig. 4a). Based on the parametric studies, N=8, r_p = 4.76mm and ρ_p=1/6 are chosen as optimal values in the subsequent studies. As revealed in Figs. 4(a, b), an increase in r_p for a given (r_r, h_p) or in h_p for a given (r_r, r_p) will result in a smaller thrust force since an increase in the PM radius r_p for a specified rotor radius r_r can be achieved but at the expense of reducing N or the number of PMs in one helix cycle (17a).

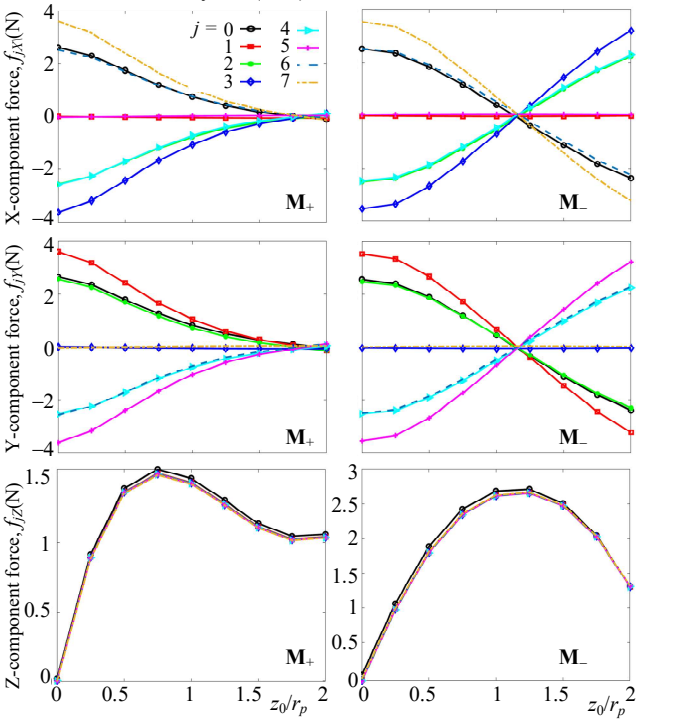

Fig. 3. Forces $\mathbf{f}_0$ contributed by each translator PM. Left: PM ($\mathbf{M}_+$). Right: PM ($\mathbf{M}_-$). Top, middle, bottom rows: X, Y, Z component forces.

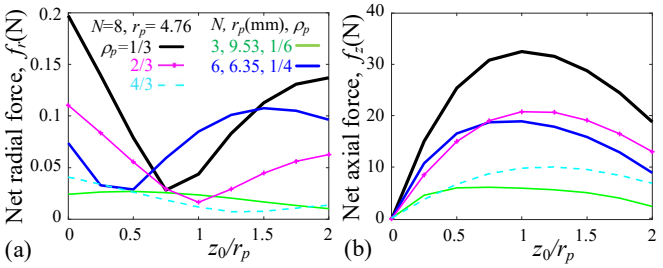

Fig. 4. Parametric effects on the forces acting on the translator. (a) Net radial forces. (b) Net axial forces.

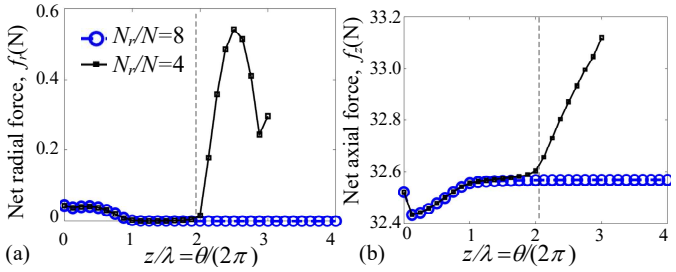

Fig. 5. End effects on the forces acting on the translator, N_t=N. (a) Net radial forces. (a) Net axial forces.

Figure 5 illustrates the end effects on the radial and axial forces by comparing two different rotor lengths (characterized by N_r/N= 4 and 8 for a given $N_t = N$). In both configurations, the radial forces are several orders smaller than their axial forces but nonzero at starting. For $N_r/N\to\infty$, the axial force approaches a constant value after rotating 2 cycles (or translating 2λ). The unbalanced radial and axial forces can be observed after translating 2λ for N_r/N=4; this is because an increasing number of the translator PMs will face air instead of rotor-PMs, where the magnitudes of the unbalanced forces depend on the PM aspect ratios and the magnetic lead (Fig. 4). For the selected design parameters, the unbalanced radial forces can be kept within 0.6N and axial forces within 2% variation of the nominal value of 32.55N over the range of 3λ.

B. Translator MFD Field (Forward) Model

To provide the theoretical basis to design an embedded sensing system for the MLS, the MFD field of the translator PMs is analyzed numerically. With ρ_t=3.73 and ρ_λ=6, the computed B_{zj} curves of each PM (j=0, 1, …, 7) with $\mathbf{M}_+$ are graphed in Fig. 6(a, top), which exhibit an identical shape but a phase difference of λ/N_t between the j^{th} and the $(j+1)^{\text{th}}$ PMs. As shown in Fig. 6(a, bottom) where the individual contributions from the $(j=0)^{\text{th}}$ PM-pair $\mathbf{M}_\pm$ and their sum are graphed, the two MFD curves are vertically symmetric with a phase difference of $2(r_p+g_z)/\lambda$ geometrically designed for the MLS. The net MFD field of the N (=8) PM-pairs is compared in Fig. 6(b); contrasting B_{zt}, (B_{xt}, B_{yt}) are non-symmetric.

The (ρ_t, ρ_λ) parametric effects on the net MFD field of the N=8 PM-pairs are illustrated on the (top, bottom) plots of Figs. 6(c, d). As shown in Fig. 6(c, top) and Fig. 6(d), the B_{zt} curves are symmetric with two local minimums at $\pm d_l/\lambda$ about the peak B_{ztj}/B_0 values at $-0.4333(Z-Z_s)/\lambda$ and the distance d_l/λ increases with ρ_t. The effects of ρ_λ on the peak B_{ztj}/B_0 values and the locations of the two local minimums at $\pm d_l/\lambda$ can be analyzed in Fig. 6(c, bottom) and Fig. 6(d).

C. Embedded Sensing System based on Translator MFD

The numerical findings in *Section III.B* provide a basis for designing an embedded sensing system for an MLS. Both the forward model (15c, d) and its inverse solutions are needed for designing an embedded field-based sensing system. While the former (*Section III.B*) offers a means to analyze the MFD field for a design, the latter that solves for the displacement from the MFD measurements must be computed in real-time, which are illustrated in Subsections *C.1* (Figs. 6, 7) and *C.2* (Fig.8).

C.1 Inverse MFD model and its non-uniqueness

Unlike the forward $\mathbf{B}_t$ model (Fig. 6b) which has a unique solution for a specified Z, the inverse solution that solves for the displacement Z from a single MFD (B_{tX}, B_{tY}, B_{tZ}) measurement may not be non-unique. As an illustration, consider two sensors (S_1 and S_2, each monitoring a range of 1.8λ) are placed along the centerline defined by (20a, b):

$$Z_{s1} = (0.9+0.43)\lambda = 1.33\lambda; \quad Z_{s2} = (1.8+1.33)\lambda = 3.13\lambda \qquad (20a, b)$$

The sensors rotate with the rotor about the Z-axis, which takes advantage of the symmetry and largest monotonic range of the B_{zt} curves (top right, Fig. 6) to cover a 3.6λ sensing range:

$$\left|B_{sl}\right|_{xy} = \sqrt{B_{xsl}^2 + B_{ysl}^2} \text{ where } l = 1,\ 2 \qquad (21a)$$

$$\text{and } \begin{bmatrix} B_{xsl}(Z,\theta) \\ B_{ysl}(Z,\theta) \end{bmatrix} = \begin{bmatrix} C_\theta & S_\theta \\ -S_\theta & C_\theta \end{bmatrix} \begin{bmatrix} B_{xtl}(Z) \\ B_{ytl}(Z) \end{bmatrix}. \qquad (21b)$$

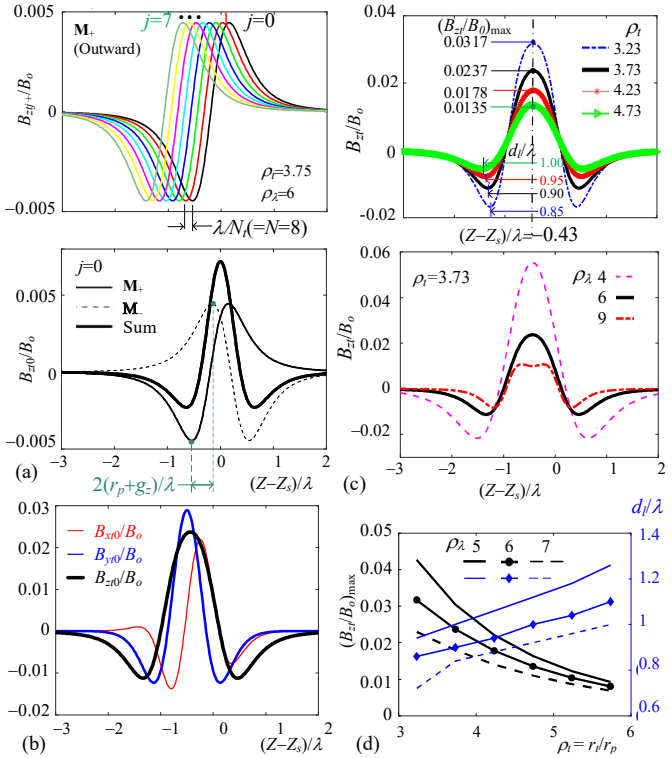

Fig. 6 Translator PM magnetic fields. (a, top) B_{tZ} from individual PMs (j=0, 1, …, 7) with M_+. (a, bottom) Individual (M_+ and M_-) from the (j=0)th PM-pair and their sum. (b) Net MFD field of the N =8 PM-pairs. (c, d) Effects of (ρ_t, ρ_λ) on B_{zt}, its peak values, and field distributions.

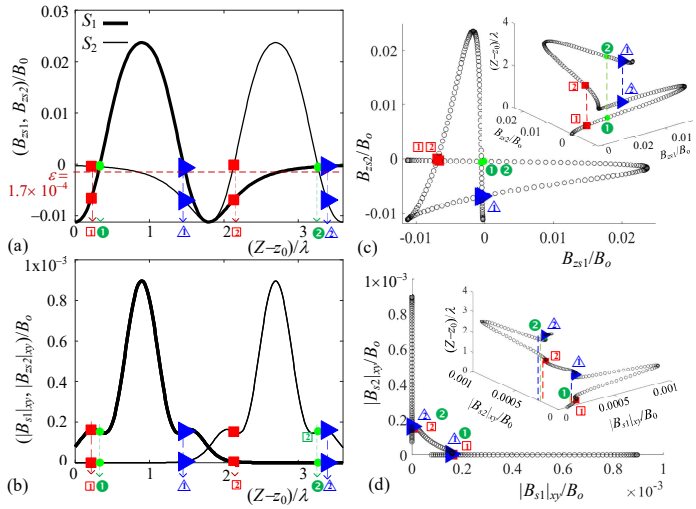

Fig. 7. Simulations illustrating the non-uniqueness of the solutions to the MFD model. (a) Axial components. (b) Radial components. (c, d) 3D view and its projection: (c) B_{zs1} and B_{zs2}. (d) $|B_{s1}|_{xy}$ and $|B_{s2}|_{xy}$.

Although the (B_{xsl}, B_{ysl}) components of the l^{th} sensor depend on both (Z, θ), the magnitude of radial component $|B_{sl}|_{xy}$ and the axial component B_{zsl} are preserved under rotation; the latter provides a means to decouple the measuring of the translation Z from that of the rotation θ. The "(S_1, S_2) measurements" are simulated to solve for the displacement Z in Fig. 7(a, b). To help visualize the non-uniqueness of the inverse solutions that solve for the normalized displacement $(Z–z_0)/\lambda$ from the $(B_{zs1}, B_{zs2})/B_o$ and/or $(|B_{s1}|_{xy}, |B_{s2}|_{xy})/B_o$ measurements, Figs. 7(c, d) present the inverse solutions to the MLS field model in 3D view and its projection on the measurement plane. Figure 7 reveals three pairs of nonunique inverse-solutions (indicated as "squared 1", triangled 2", and circled 3"; in other words, two possible displacements for each of the three (B_{zs1}, B_{zs2}) pairs labeled as red-squares, blue-triangles, and green-dots, respectively.

C.2 Measurement algorithm for embedded (Z, θ) sensing

To eliminate the ambiguity from the inverse solutions, the full motion range is divided into four domains (Γ_1, Γ_2, Γ_3, Γ_4) based on B_Σ (= B_{zs1}+B_{zs2}) such that the inverse solution in each domain is monotonic and can be uniquely determined from the measured $\mathbf{B}_{s1}$ and $\mathbf{B}_{s2}$ using the three-step sensing algorithm (Fig. 8d) to independently measure Z and θ.

Step 1: determine the domain using logical deduction (Fig. 8b):
If $|B_{s1}|_{xy} \geqslant |B_{s2}|_{xy}$: if $B_{zs2} \geqslant e \rightarrow \Gamma_1$; else $B_{zs2} < e \rightarrow \Gamma_2$.
else $|B_{s1}|_{xy} < |B_{s2}|_{xy}$: if $B_{zs1} < e \rightarrow \Gamma_3$; else $B_{zs1} \geqslant e \rightarrow \Gamma_4$.

Step 2: determine Z from the calibrated curve (inverse model) within the domain found in Step 1 (Fig. 8b).

Step 3: from the coordinate transformation (21b),

$$\theta = \tan^{-1}\frac{B_{xsl}}{B_{ysl}} - \tan^{-1}\frac{B_{xtl}}{B_{ytl}};\ l = \begin{cases} 1 & |B_{s1}|_{xy} \geq |B_{s2}|_{xy} \\ 2 & |B_{s1}|_{xy} < |B_{s2}|_{xy} \end{cases} \qquad (22)$$

As illustrated in Fig. 8(c), the radial (B_{xtl}, B_{ytl}) component of the l^{th} sensor depends only on Z and thus serves as a reference to compute θ from (B_{xsl}, B_{ysl}). The sign (and hence uniqueness) of θ in (22) is determined from the signed (B_{xsl}, B_{ysl}) and (B_{xtl}, B_{ytl}).

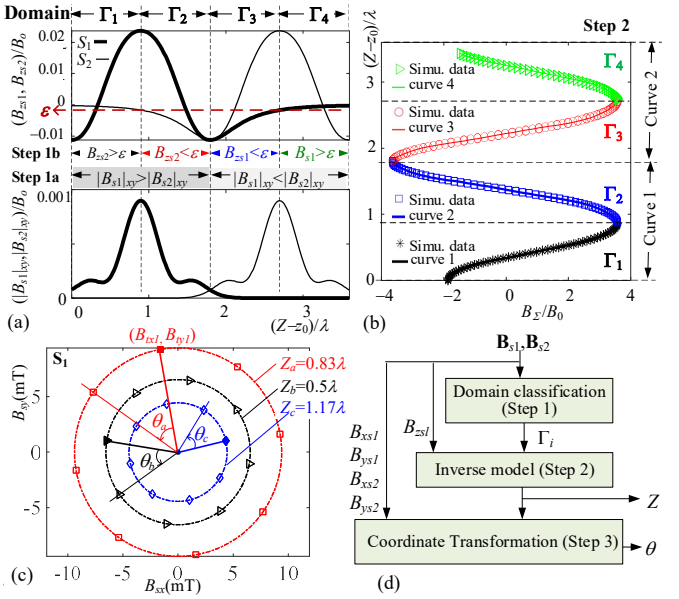

Fig. 8. Simulations illustrating the embedded sensing system. (a, b) Domain classification and inverse solutions based on B_Σ (= B_{zs1}+B_{zs2}). (c) Inverse θ solution. (d) Flowchart of the sensing algorithm.

IV. EXPERIMENT RESULTS AND DISCUSSION

Based on the parametric studies in *Section III*, a prototype MLS with embedded sensing has been designed (Fig. 9) and developed (Fig. 10). The rotor (N_r = 32 PM-pairs) is supported on two rotary bearings at both ends of the rotor, and the translator (N_t=N = 8 PM-pairs) slides along a pair of alignment rods in the bushing bearings. The PM-pairs are mechanically located so that the same magnetic lead between the rotor and translator can be maintained at both the start and the end of the travel to generate the positive (or negative) thrust force in the forward (or backward) direction (Fig. 9c) where the translator-PMs are ahead by z_0 relative to the corresponding rotor-PMs in

its motion direction. The characteristic parameters of the MLS and its embedded sensors, and the instrumentation used for the experimental studies are summarized in Table II. The results are presented in *Section IV.A* and discussed in *Section IV.B*.

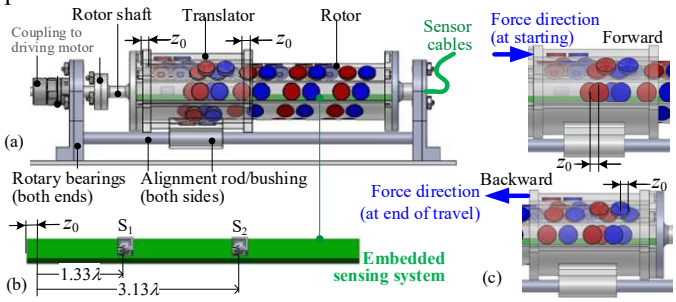

Fig. 9 CAD model of the prototype MLS.

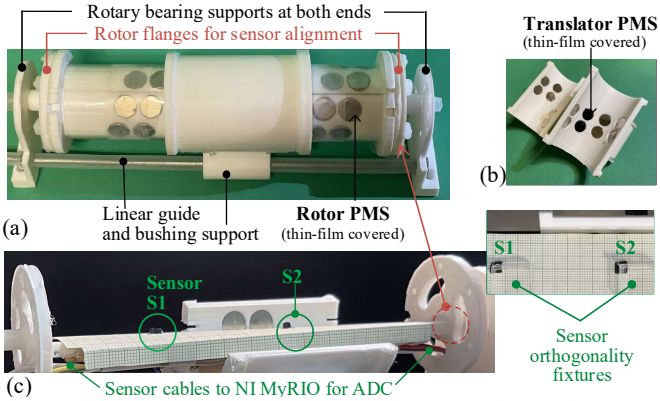

Fig. 10. Prototype MLS. (a) Overall view and rotor PMs. (b) Translator PMs. (c) Embedded sensors.

A. Experimental Results

The study with results in Figs. 11~14 and Table III has a three-folded objective: The 1st verifies the DCS model by comparing its calculated MFD field **B** of a PM in the global coordinates with the Biot-Savart's integral [15] and manufacturer's experimental data [17] in Fig. 11 where %RMSE is the root-mean square error. The 2nd and 3rd calibrate and validate the embedded sensing system, respectively.

The 2nd study calibrates the sensing system (Fig. 12a), where the two sets of three single-axis Hall-effect sensors (S_1, S_2) are fixed at $Z = 1.33\lambda$ and 3.13λ on the centerline, each set measuring (B_{sx}, B_{sy}, B_{sz}) of the PMs positioned by a XYZ micro-position stage. To cover the same MFD measuring range of the prototype MLS, two PMs with the same radius r_p= 4.76mm but large aspect ratios are used in the calibration. During calibration, the measured output voltages (offset subtracted) of each sensor are digitized by an NI MyRIO and processed in NI LabVIEW, which are then linearly related to the MFD measured by a handheld Gaussmeter in Fig. 12(a).

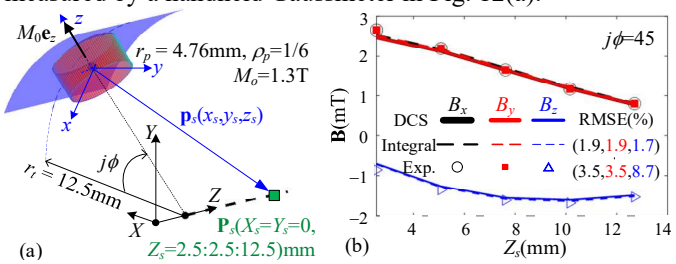

Fig. 11. Comparison of DCS model with analytical solutions and manufacturer's data (a) Coordinate systems. (b) Results.

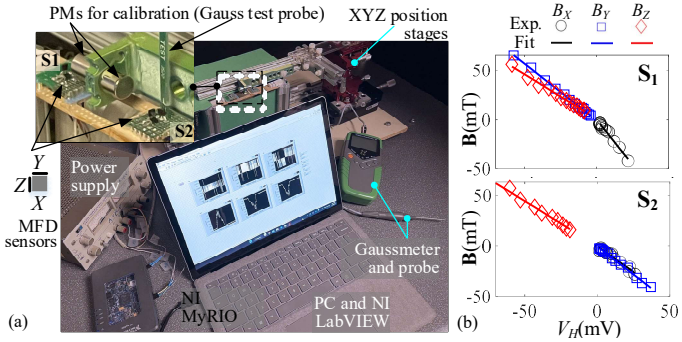

Fig. 12 MLS sensor calibration. (a) Experiment setup. (b) Results.

Table II. Parameters of the MLS, embedded sensor, and testbed

Instrumentation	Specification
Gaussmeter	0-2400mT, Relative error: ±2%
XYZ μStage (HTIMS502R)	Range: 25.4mm. Resolution: 1μm
Rotary μStage (HTIMS502R)	Range: 360°. Resolution: 1°/60.
Linear μMeter	Range: 25.4mm. Resolution: 2.54μm
Embedded sensors and DAQ	
MFD sensors (CYSJ166A)	Range: 3T. Sensitivity 3.1~4.1mV/mT
ADC (NI MyRIO)	12-bit Analog input (0 ~ 5V)
Optimized MLS Geometry	
$\rho_r = 3$, $\rho_t = 3.73$, $\rho_z = 0.17$, $\rho_\lambda = 6$. $N = 8$, $N_t/N = 1$, $N_r/N = 4$, $z_0/r_p = 1$	

Table III: Experimental results

Sensor calibration (at supply voltage: 5.83V) $B_i = m_H V_H + c_H$ **(Fig. 12)**

Sensors	$X(m_H, c_H)$	$Y(m_H, c_H)$	$Z(m_H, c_H)$
S_1	(–1.856, 0.594)	(–1.154, –1.684)	(–0.906, 1.049)
S_2	(–1.021, –0.255)	(–1.119, 0.732)	(–0.889, 2.578)

Domain curve fits: (Fig. 12c) $Z(B) = c_4B^4 + c_3B^3 + c_2B^2 + c_1B + c_0$	$\lvert\mathbf{B}_s\rvert_{xy}$ **mean, STD (Fig. 12e)**
Curve 1 (C1): [0.040 0.054 0.009 –0.006 0.001]	Z=0.522λ
Curve 2 (C2): [1.082 –0.035 0.000 0.000 0.000]	(8.418 ,0.530)
Curve 3 (C3): [1.918 0.037 0.003 0.000 0.000]	Z=2.3λ
Curve 4 (C4): [2.917 –0.054 0.044 –0.015 0.001]	(6.786, 1.121)

Estimation error (Ave, SD, Max):

$\lvert\Delta B_z\rvert$ (mT): S1(0.56, 0.18, 1.88); and S2 (0.40, 0.29, 1.99)

$\left\lvert\Delta Z/\lambda\right\rvert$: (0.05, 0.06, 0.14) $\qquad$ $\left\lvert\Delta\theta/2\pi\right\rvert$: (0.05, 0.04,0.12)

The 3rd study validates the embedded sensing system for measuring Z on the setup shown in Fig. 13(a) where the measurements are digitized by MyRIO, analyzed via LabVIEW (Fig. 12a) and summarized in Figs. 13(b~e). The measured (B_{zs1}, B_{zs2}) are plotted in Fig. 13(b) over the 3λ range in the step of 45° for θ=0° to 315°, demonstrating the measured (B_{zs1}, B_{zs2}) do not depend on θ. Their sums, B_Σ (= B_{zs1}+B_{zs2}), for domain classification are plotted in Fig. 13(c) where the DCS model and domain curve-fits (Table III) are compared with experimental data (θ=0 as an example). Figure 13(d) plots the (B_{xs}, B_{ys}) components which depend on both the displacement and rotation for two angles (θ=0°, 45°). Once Z is acquired, the corresponding (B_{tx}, B_{ty}) are computed to determine θ (Fig. 13e).

B. Discussion of Results

The comparisons among the DCS model, integral solutions, and experimental data in Fig. 11, in general, show very good agreements. The %RMSE of the (B_X, B_Y, B_Z) relative to the experimental data and integral solutions are (3.55%, 3.55%, 8.74%) and (1.91%, 1.91%, 1.71%), respectively. The experimental (B_X, B_Y, B_Z) data exhibit a slightly larger RMSE

than the integral solutions and the DCS model, suggesting that the actual PM properties are slightly different from the manufacturer's specification assumed in the analytical models.

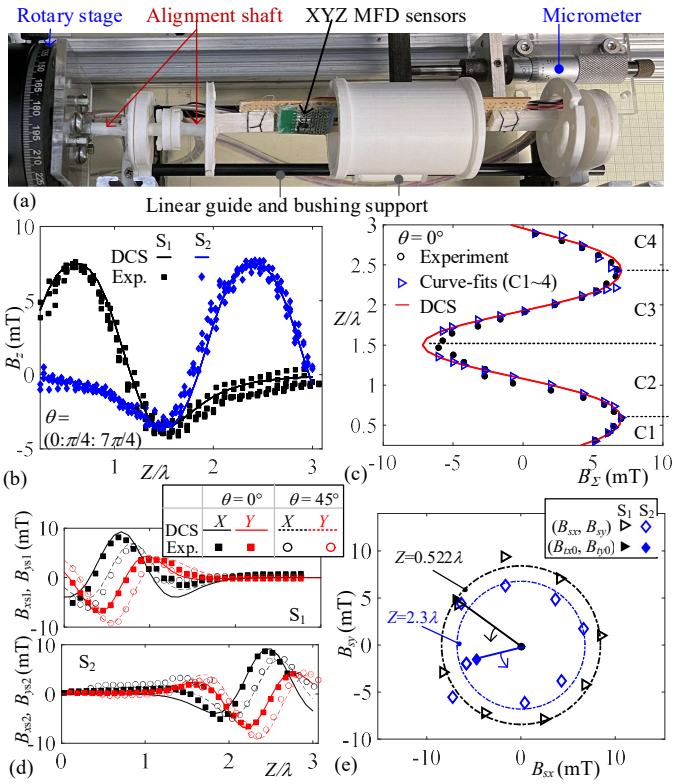

Fig. 13 Experiment Results. (a) Setup. (b) B_{zs1}, B_{zs2}. (c) $B_{\Sigma}= B_{zs1}+B_{zs2}$. (d) B_{xsl} and B_{ysl} where l=1 and 2. (e) Illustrative θ inverse solutions.

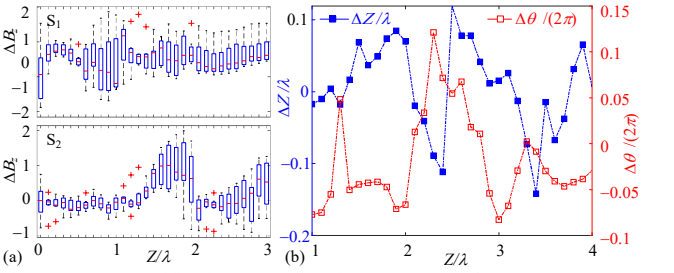

Fig. 14 Error quantification. (a) z-direction MFD error (b) Z-θ error.

Figure 14(a) graphs the boxplots showing the (Ave, SD, Max) errors, where data were taken at 8 different angles at each Z/λ location, from which the absolute sensing errors [$|\Delta\mathbf{B}|$mT, $\Delta Z/\lambda$, $\Delta\theta/(2\pi)$] are statistically summarized in Table III. Fig. 14(b) shows the displacement/rotation errors over the 3λ range. The displacement Z (Ave, SD, Max) errors are (5%, 6%, 14%)λ with its largest value at about 1.5λ, which are due primarily to the MFD sensing errors (Table III) and a small sensitivity of the MFD sensor at 1.5λ. Because the θ sensing depends on the Z sensing, it is less accurate than the latter. Some discrepancies can also be observed in Fig. 13(e) where the radial (B_{xtl}, B_{ytl}) component of the l^{th} sensor depends only on Z and should appear on the circle for a specified Z; the radial variations from its mean are caused by sensor misalignments. The sensing errors can be reduced by improving the mechanical hardware alignments to ensure orthogonality and by employing MFD sensors that have a higher sensitivity and low sensing noise.

V. CONCLUSION

The modeling, design, and parametric studies of an MLS with embedded sensing have been presented. The MFD and force models of an MLS have been formulated in a closed form neither assuming an ideal gear ratio nor neglecting the end effects. The DCS model reveals that B_{sz} and $|B_s|_{xy}$ along the translator centerline are invariant to θ, which leads to the development of a prototype MLS with an embedded field-based sensing system and a 3-step algorithm to determine the uniqueness of the inverse solution for independently measuring Z and θ. The DCS models and sensor design have been experimentally validated. The comparisons between the DCS model and experimental data show excellent agreement. The (Ave, SD, Max) RMS errors of the absolute displacement and rotation estimation errors are (5%, 6%, 14%) of the pitch λ, and (5%, 4%, 12%) of 2π, respectively.

REFERENCES

[1] M. Carpita, T. Beltrami, C. Besson, S. Gavin, "Multiphase active way linear motor: proof-of-concept prototype," *IEEE Trans. Ind. Electron*., v. 59, n. 5, pp. 2178–2188, 2012.

[2] R. Cao, M. Cheng, B. Zhang, "Speed control of complementary and modular linear flux-switching permanent-magnet motor," *IEEE Trans. Ind. Electron.*, v. 62, n. 7, pp. 4056–4064, 2015.

[3] S. H. Hosseinnejad, T. F. Besier, A. J. Taberner, B. P. Ruddy, "Design optimization of a direct-drive linear actuator assistive device for stroke," *IEEE/RSJ Int. Conf. on Intel. Robots and Sys. (IROS)*, pp. 6349-6354, 2017.

[4] P. Jain, T. K. Bera, A. Singla, M. Isaksson, "Linear actuator–based knee exoskeleton for stand–sit–stand motions: a bond graph approach," *Simulation*, v. 98, n. 8, pp. 627-644, 2022.

[5] N. I. Berg, R. K. Holm, P. O. Rasmussen, "A novel magnetic lead screw active suspension system for vehicles," *IEEE Energy Convers. Cong. and Expo. (ECCE)*, pp. 3139–3146, 2014.

[6] L. Zhu, C. Ma, W. Li, "A novel structure of electromagnetic lead screw for wave energy converter," *Energies*, v. 15, n. 8, 2022.

[7] A. Heya, Y. Nakata, M. Sakai, H. Ishiguro, K. Hirata, "Force estimation method for a magnetic lead-screw-driven linear actuator," *IEEE Trans. Mag.*, v. 54, n. 11, pp. 1–5, 2018.

[8] L. Bu, Y. Fujimoto, "Novel Force estimation method for magnetic leadscrew based Rotin actuator," *IEEE Tran. Ind. App.*, pp 1-11, 2022.

[9] J. Wang, G. W. Jewell, D. Howe, "A general framework for the analysis and design of tubular linear permanent magnet machines," *IEEE Trans. Mag.*, v. 35, n. 3, pp. 1986–2000, 1999.

[10] J. Wang, K. Atallah, W. Wang, "Analysis of a magnetic screw for high force density linear electromagnetic actuators," *IEEE Trans. Mag.*, v. 47, n. 10, pp. 4477–4480, 2011.

[11] S. Pakdelian, N. W. Frank, H. A. Toliyat, "Magnetic design aspects of the trans-rotary magnetic gear," *IEEE Trans. Energy Convers.*, v. 30, n. 1, pp. 41–50, 2015.

[12] Z. Ling, J. Ji, J. Wang, W. Zhao, "Design optimization and test of a radially magnetized magnetic screw with discretized PMs," *IEEE Trans. Ind. Electron*., v. 65, n. 9, pp. 7536–7547, 2018.

[13] C.-Y. Lin, K.-M. Lee, B. Hao, "Distributed current source method for modeling magnetic and eddy-current fields induced in non-ferrous metallic objects," *IEEE/ASME Trans. Mechatronics*, v.23, n.3, pp.1038-1049, 2018.

[14] B. Hao, K.-M. Lee, K. Bai, "Distributed current source modeling method for 3d eddy current problem in magnetic conductor with j-φ formulation," *J. of Comp. Physics*, v. 401, n. 15, 109027(16 pages), 2020.

[15] J.-Y. Lim, K.-M. Lee, "Distributed multi-level current models for design analysis of electromagnetic actuators," *IEEE/ASME Trans. Mechatronics*, v. 20, no. 5, pp. 2413-2424, 2015.

[16] J.-Y. Lim, K.-M. Lee, "Design of electromagnetic actuators using layout optimization with distributed current source models," *IEEE/ASME Trans. Mechatronics*, v. 20, n. 6, pp 2726-2735, 2015.

[17] https://www.kjmagnetics.com/fieldcalculator.asp, K&J Magnetics, Inc.